

REPORT DOCUMENTATION PAGE

Form Approved  
OMB No 0704-0188

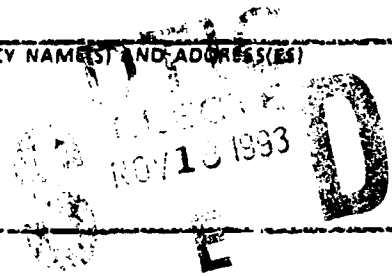
2

AD-A272 910



Information is estimated to average 1 hour per response, including the time for reviewing instructions, searching existing data sources, gathering and reviewing the collection of information, sending comments regarding this burden estimate or any other aspect of the collection of information, including suggestions for reducing this burden, to Washington Headquarters Service, Directorate for Information Operations and Reports, 1215 Jefferson Avenue, Washington, DC 20540, and to the Office of Management and Budget, Paperwork Reduction Project (0704-0188), Washington, DC 20503.

1. REPORT DATE 10/25/93		2. REPORT TYPE AND DATES COVERED Final - 11/1/89 - 6/30/93	
4. TITLE AND SUBTITLE "Scanning Tunneling Microscopy Investigations of Metal Dichalcogenide Materials."		5. FUNDING NUMBERS 61102F 2303/BS	
6. AUTHOR(S) Charles M. Lieber		8. PERFORMING ORGANIZATION REPORT NUMBER	
7. PERFORMING ORGANIZATION NAME(S) AND ADDRESS(ES) Department of Chemistry Columbia University New York, NY 10027		10. SPONSORING/MONITORING AGENCY REPORT NUMBER AFOSR-90-0029	
9. SPONSORING/MONITORING AGENCY NAME(S) AND ADDRESS(ES) AFOSR/NC Building 410 Bolling AFB, DC 20332-6448		11. SUPPLEMENTARY NOTES	
12a. DISTRIBUTION/AVAILABILITY STATEMENT Approved for public release; distribution is unlimited.		12b. DISTRIBUTION CODE	
13. Title: "Scanning Tunneling Microscopy Investigations of Metal Dichalcogenide Materials" Abstract Scanning tunneling microscopy (STM) and atomic force microscopy (AFM) have been used to characterize the atomic level structure of electronic properties, reactivity and wear of metal dichalcogenide materials that are or have potential as solid state lubricants. Single crystals of MoS <sub>2</sub> , Ni <sub>x</sub> Mo <sub>1-x</sub> S <sub>2</sub> , MoS <sub>2-x</sub> Se <sub>x</sub> and MoS <sub>2-x</sub> Te <sub>x</sub> have been prepared to determine how chemical modifications affect the local structure and electronic properties of this lubricant. STM images of Ni-doped MoS <sub>2</sub> show localized electronic states due to the Ni atoms, while images of Se- and Te-doped materials indicate that anion substitution is electronically delocalized. AFM studies of Te-doped MoS <sub>2</sub> show, however, that the tellurium dopants form atomic scale structural protrusions that may reduce sliding friction. AFM has also been used to characterize nanometer scale wear and oxidation on MoS <sub>2</sub> and NbSe <sub>2</sub> surfaces. In atmosphere at room-temperature AFM studies showed that NbSe <sub>2</sub> wears approximately three times faster than MoS <sub>2</sub> . Furthermore, oxidation studies demonstrated that NbSe <sub>2</sub> was significantly more reactive than MoS <sub>2</sub> with molecular oxygen. These results indicate that the intrinsic stability of the MoS <sub>2</sub> surface make it an effective lubricant. AFM was also used to elucidate the growth of MoO <sub>3</sub> on the surface of MoS <sub>2</sub> during oxidation, and to study wear properties of these MoO <sub>3</sub> crystallites. The AFM tip was used to define lines with 10 nm resolution in MoO <sub>3</sub> and to manipulate distinct MoO <sub>3</sub> structures on the MoS <sub>2</sub> surface. In addition, metal-substitution in TaS <sub>2</sub> has been studied systematically using STM and theoretical methods. Investigations of Nb-doped materials provide the first direct structural evidence for weak pinning of an electronic lattice, and furthermore, theoretical analyses have led to the discovery of a new phase, the hexatic, in these materials.			
14. SUBJECT TERMS scanning tunneling microscopy, atomic force microscopy, metal dichalcogenide, metal doping, structure, wear, oxidation.		15. NUMBER OF PAGES 45	
17. SECURITY CLASSIFICATION OF REPORT Unclassified		18. SECURITY CLASSIFICATION OF THIS PAGE Unclassified	
19. SECURITY CLASSIFICATION OF ABSTRACT Unclassified		20. LIMITATION OF ABSTRACT Unlimited	



**Best  
Available  
Copy**

## Table of Contents

<u>Section</u>		<u>Page</u>
	LIST OF ILLUSTRATIONS .....	4
1.	INTRODUCTION.....	5
2.	STRUCTURE AND ELECTRONIC PROPERTIES OF METAL DICHALCOGENIDE MATERIALS .....	7
	2.1 Experimental Methods .....	7
	2.2 Ni-Doped MoS <sub>2</sub> .....	9
	2.3 Anion-Doped MoS <sub>2</sub> .....	12
3.	REACTIVITY AND WEAR OF MoS <sub>2</sub> AND NbSe <sub>2</sub> .....	15
	3.1 Wear of MoS <sub>2</sub> Versus NbSe <sub>2</sub> .....	15
	3.2 Oxidation of MoS <sub>2</sub> Versus NbSe <sub>2</sub> .....	17
	3.3 Wear and Nanofabrication .....	22
4.	METAL-SUBSTITUTED TANTALUM DISULFIDE.....	26
	4.1 Introduction .....	26
	4.2 STM Characterization .....	27
	4.3 Theoretical Analysis.....	34
5.	SUMMARY .....	42
6.	ACKNOWLEDGMENTS.....	43
7.	REFERENCES.....	44

Accession For	
NTIS CRA&I	<input checked="" type="checkbox"/>
DTIC TAB	<input type="checkbox"/>
Unannounced	<input type="checkbox"/>
Justification	
By .....	
Distribution /	
Availability Codes	
Dist	Available for Special
<b>A-1</b>	

DTIC QUALITY INSPECTED 5

**93-28114**



*4428*

93 11 16 053

## List of Illustrations

<u>Figure</u>		<u>Page</u>
1-1	Schematic side-view of MoS <sub>2</sub> .....	5
2-1	Illustration of the STM System.....	8
2-2	Schematic of the AFM.....	9
2-3	STM Images of Ni <sub>x</sub> Mo <sub>1-x</sub> S <sub>2</sub> .....	11
2-4	Schematic of Anion-Doped MoS <sub>2</sub> .....	12
2-5	STM/AFM images of MoS <sub>1.75</sub> Se <sub>0.25</sub> .....	13
2-6	STM/AFM images of MoS <sub>1.75</sub> Te <sub>0.25</sub> .....	14
3-1	Wear of NbSe <sub>2</sub> and MoS <sub>2</sub> Surfaces.....	16
3-2	Oxidation of MoS <sub>2</sub> at 440°C.....	17
3-3	Oxidation of NbSe <sub>2</sub> at 220°C.....	18
3-4	Oxidation of MoS <sub>2</sub> at 400 and 420°C.....	19
3-5	Oxidation of MoS <sub>2</sub> at 440, 460 and 480°C.....	20
3-6	Time Dependence of MoS <sub>2</sub> Oxidation.....	21
3-7	Schematic of MoS <sub>2</sub> Following Oxidation.....	22
3-8	Nanomachining of MoO <sub>3</sub> .....	24
3-9	Manipulation of Nanometer Structures.....	25
4-1	STM Image of TaS <sub>2</sub> at 360K.....	28
4-2	STM Images of Nb <sub>x</sub> Ta <sub>1-x</sub> S <sub>2</sub> : x = 0.02 and 0.04.....	29
4-3	STM Images of Nb <sub>x</sub> Ta <sub>1-x</sub> S <sub>2</sub> : x = 0.07 and 0.10.....	31
4-4	Triangulation of STM Images of Nb <sub>x</sub> Ta <sub>1-x</sub> S <sub>2</sub> .....	33
4-5	Structure Factors for Nb <sub>x</sub> Ta <sub>1-x</sub> S <sub>2</sub> Materials.....	36
4-6	Radial Distribution Functions for Nb <sub>x</sub> Ta <sub>1-x</sub> S <sub>2</sub> Materials.....	38
4-7	Translational and Orientational Correlation Functions.....	40

## Section-1

### INTRODUCTION

The transition metal dichalcogenide ( $\text{MX}_2$ ) materials, and in particular  $\text{MoS}_2$ , have been one of the most widely studied classes of solid lubricants.<sup>1-8</sup> In general, the effective lubricating properties of  $\text{MoS}_2$  have been attributed to the highly anisotropic structure of this material (Fig. 1-1).<sup>3,4</sup>

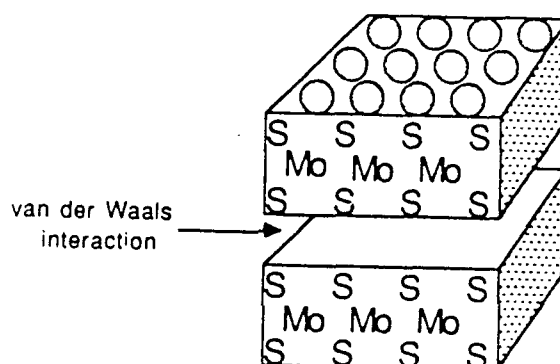


FIGURE 1-1. Schematic side-view of the  $\text{MoS}_2$  structure illustrating covalently bonded S-M-S layers that interact primarily through dispersion forces.

The weak interlayer (S-Mo-S)/(S-Mo-S) interactions enable facile interlayer shear, and hence lead to a small coefficient of friction. However, factors in addition to the layered structural motif must also be important since many structurally similar  $\text{MX}_2$  solids (e.g.,  $\text{NbSe}_2$ ) are poor lubricants. Other factors believed to play a role in determining the overall effectiveness of a lubricant include: (1) the electronic structure of the solid; (2) adhesion of the lubricant to the substrate (metallic) interface, and (3) reactivity and wear of the lubricant surface. In the case of  $\text{MoS}_2$  and  $\text{NbSe}_2$ , photoelectron spectroscopy data and molecular orbital analyses have been used to argue that electronic structure can affect significantly the interlayer

shear.<sup>3,4</sup> Specifically, long-range interlayer interactions between the half-filled Nb-dz<sup>2</sup> orbitals in NbSe<sub>2</sub> may inhibit interlayer shear relative to MoS<sub>2</sub>. Alternatively, it is also possible that the electronic properties of NbSe<sub>2</sub> promote deleterious surface reactions (and thus wear) or reduce the binding interaction to metal substrate surfaces compared with MoS<sub>2</sub>.

To develop a microscopic understanding of MoS<sub>2</sub> and other metal dichalcogenides, which is essential for the rational design and development of new materials with improved tribological properties we have used scanning tunneling microscopy (STM) and atomic force microscopy (AFM).<sup>9-28</sup> STM and AFM provide direct atomic resolution data addressing the structural, electronic, wear and frictional properties of interfaces and as such these new techniques are essential for tribology research. In this report we summarize the first systematic application of these methodologies to the transition metal dichalcogenide materials.

**Section-2**  
**STRUCTURE AND ELECTRONIC PROPERTIES**  
**OF METAL DICHALCOGENIDES**

**2.1 EXPERIMENTAL METHODS**

The measurements made during this project were carried out on single crystal metal dichalcogenide samples. Although single crystals are experimentally difficult to prepare, they represent the best defined samples from which strong conclusions can be drawn. Facilities for single crystal growth of metal dichalcogenide solids were developed during the initial stages of the project.

Single crystals of  $\text{MoS}_2$ ,  $\text{Ni}_{0.1}\text{Mo}_{0.9}\text{S}_2$ ,  $\text{MoS}_{2-x}\text{Se}_x$  ( $x = 0.25, 0.5$ ) and  $\text{MoS}_{1.75}\text{Te}_{0.25}$  were grown from polycrystalline powders by chemical vapor transport.<sup>22</sup> For example, a stoichiometric mixture (5 g total mass) of molybdenum and sulfur was sealed in a quartz tube under vacuum and reacted for 10 days at 1000°C. Following this initial reaction, the resulting polycrystalline powder was ground resealed under vacuum in a quartz tube together with excess sulfur (60 mg) and iodine (100 mg). Single crystals were grown in a 50 - 100 °C gradient over a three-week period. The crystals obtained from the growth region had the expected plate-like layered morphology and varied in size from 1 mm x 1 mm to 3 mm x 3 mm. The metal (Ni) and chalcogenide (Se, Te) doped  $\text{MoS}_2$  crystals were grown using similar conditions. The procedures for the growth of other metal dichalcogenide samples examined during this project (e.g.,  $\text{NbSe}_2$  and  $\text{TaS}_2$ ) were also similar and have been published.<sup>11-16</sup>

Both commercial and custom STMs have been utilized in our measurements. The underlying basis for STM experiments and its application to metal dichalcogenide materials have been discussed previously in several of our published reviews.<sup>18,21</sup> The home-built ultrahigh vacuum (UHV) STM system was constructed during the project to carry out

experiments under highly controlled vacuum conditions. This instrument is illustrated in Figure 2-1.

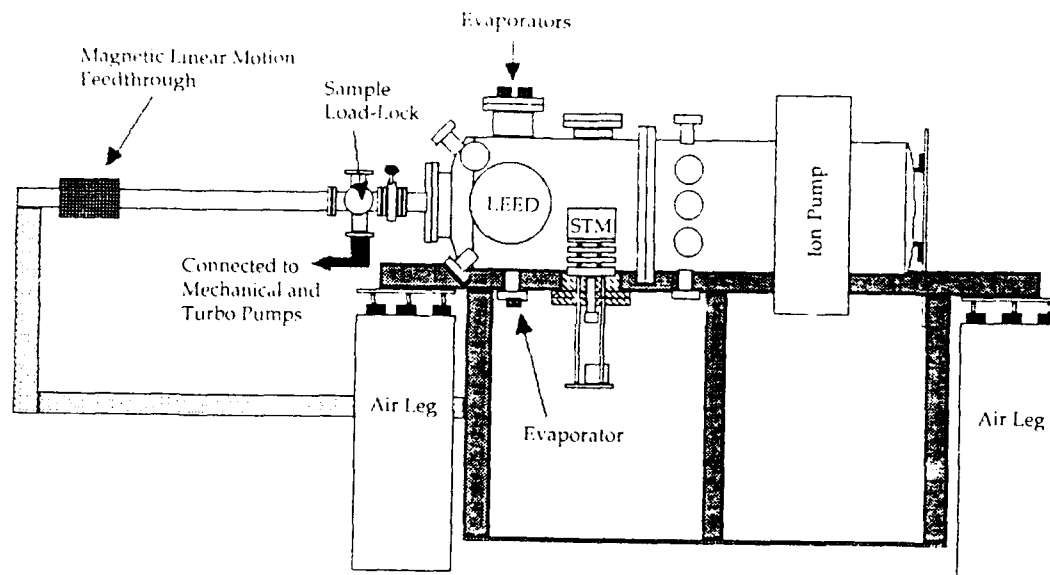


FIGURE 2-1. Schematic view of the UHV-STM system.

Preliminary studies of wear and reactivity were carried out with this instrument and are discussed below. In addition, we anticipate that this specialized instrument will be utilized extensively in our new AFOSR project.

In addition, we have developed an AFM for operation in controlled environments. In force microscopy, an interface is imaged by scanning a surface below with a probe that is attached to a cantilever; deflections of the cantilever are related to surface features. The force(s) that cause the cantilever deflections define the mode of imaging. For example, when the tip is in contact with the surface repulsive electrostatic forces usually are the dominant interaction; this contact regime is termed repulsive mode imaging. Alternatively, if the tip is removed from the surface a van der Waals attractive interaction may be the dominant force between the sample and tip; this case is termed attractive mode imaging. All of our AFM studies reviewed below were carried out in the repulsive mode using a modified commercial

instrument.<sup>46,56</sup>  $\text{Si}_3\text{N}_4$  cantilever-tip assemblies were used for both imaging and modification studies. An illustration of the experimental apparatus is shown in Figure 2-2.

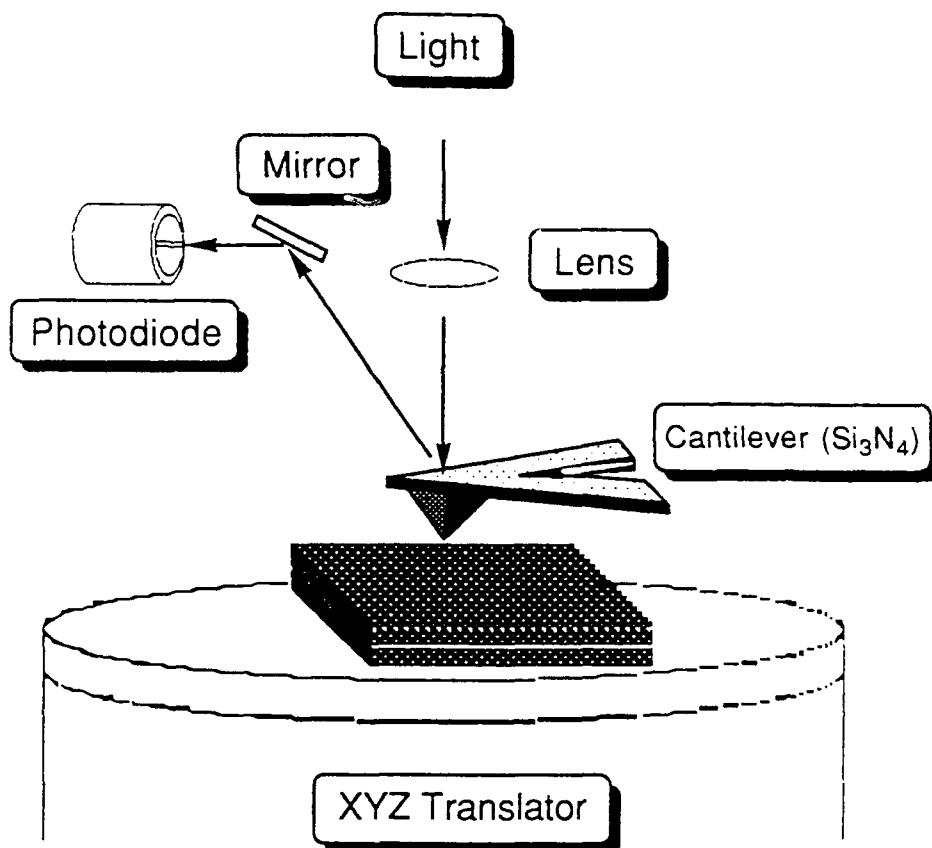


FIGURE 2-2. Schematic view of the atomic force microscope.

## 2.2 Ni-DOPED $\text{MoS}_2$

Our initial studies of the atomic level structure and electronic properties of solid lubricants focused on  $\text{MoS}_2$  and Ni-substituted  $\text{MoS}_2$   $\text{Ni}_x\text{Mo}_{1-x}\text{S}_2$ .<sup>22</sup> The Ni-doped materials are a particularly important system for high-resolution studies since recent work has shown that Ni-substitution enhances the tribological properties of  $\text{MoS}_2$  compared to the pure compound. To understand these results we have used STM and AFM to characterize the structural properties of well-defined single crystals of  $\text{Ni}_x\text{Mo}_{1-x}\text{S}_2$ . First, stoichiometric crystals with  $x(\text{Ni}) = 0, 0.02, 0.05, \text{ and } 0.10$  were synthesized. The Ni-doped materials have been characterized by a variety of techniques including variable-temperature resistivity

measurements and X-ray diffraction. These studies show that Ni-doping does not significantly alter the average structural properties of the MoS<sub>2</sub> system.

AFM images, which reflect primarily surface structure, exhibit a regular atomic lattice with a period of  $3.15 \pm 0.05 \text{ \AA}$ . This structure corresponds to the surface sulfur atom positions and is in agreement with the structure inferred from diffraction measurements. In contrast, STM images of the Ni-doped materials exhibit pronounced defects in the hexagonal atomic lattice (Fig. 2-3). Since the AFM data show conclusively that there are no large

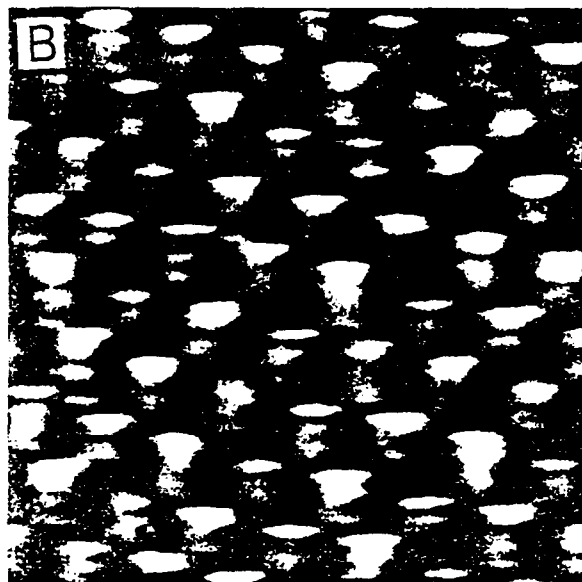
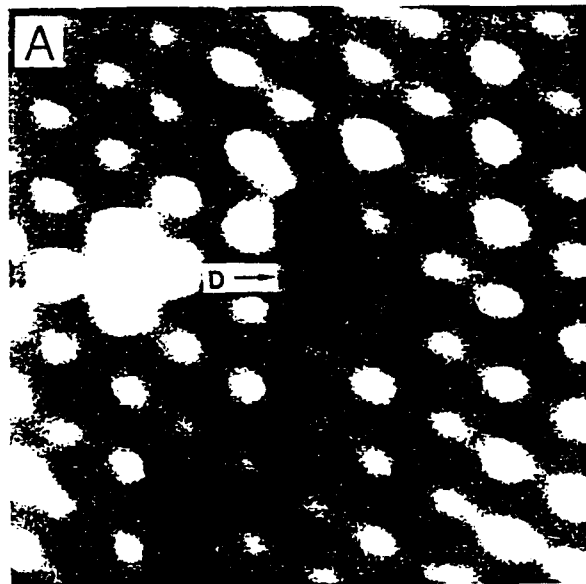


FIGURE 2-3.  $30 \times 30 \text{ \AA}^2$  gray-scale STM images of (a)  $\text{Ni}_{0.1}\text{Mo}_{0.9}\text{S}_2$ . and (b)  $\text{MoS}_2$ .

Localized effects are clearly visible in (b).

structural variations due to Ni-substitution these defects can be attributed to localized variations in the density of electronic states due to nickel atoms in the lattice. Hence, we can conclude that on an atomic scale Ni-substitution only affects electronic states near the Fermi level and does not perturb significantly the structure. Such localized changes are not expected to enhance layer-layer sliding or material plasticity, although these defects could enhance adhesion.

### 2.3 ANION-DOPED MoS<sub>2</sub>

We have also characterized the structural and electronic effects of selenium and tellurium substitution in MoS<sub>2</sub>. The initial motivation for this work was the suggestion that Se or Te dopants could function as atomic scale bearings as shown schematically in Figure 2-4.

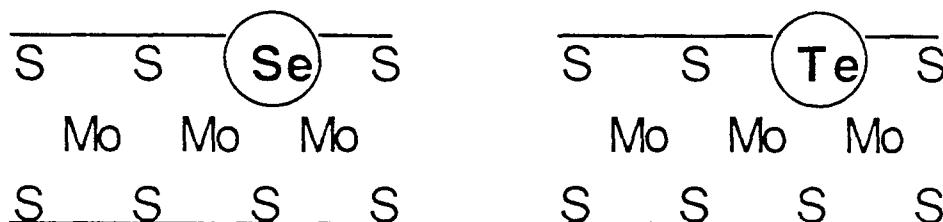


FIGURE 2-4. Schematic cross-section of MoS<sub>2</sub> substituted with Se and Te. The larger radii of these anions is highlighted.

Alternatively, it is expected that the selenium or tellurium dopants might function as good substrate anchoring sites.

STM and AFM investigations of these new materials have produced several interesting results.<sup>22</sup> Atomic resolution STM and AFM images of MoS<sub>1.75</sub>Se<sub>0.25</sub> exhibit similar hexagonal lattices with periods of  $0.32 \pm 0.01$  nm and  $0.32 \pm 0.02$  nm, respectively (Fig. 2-5).

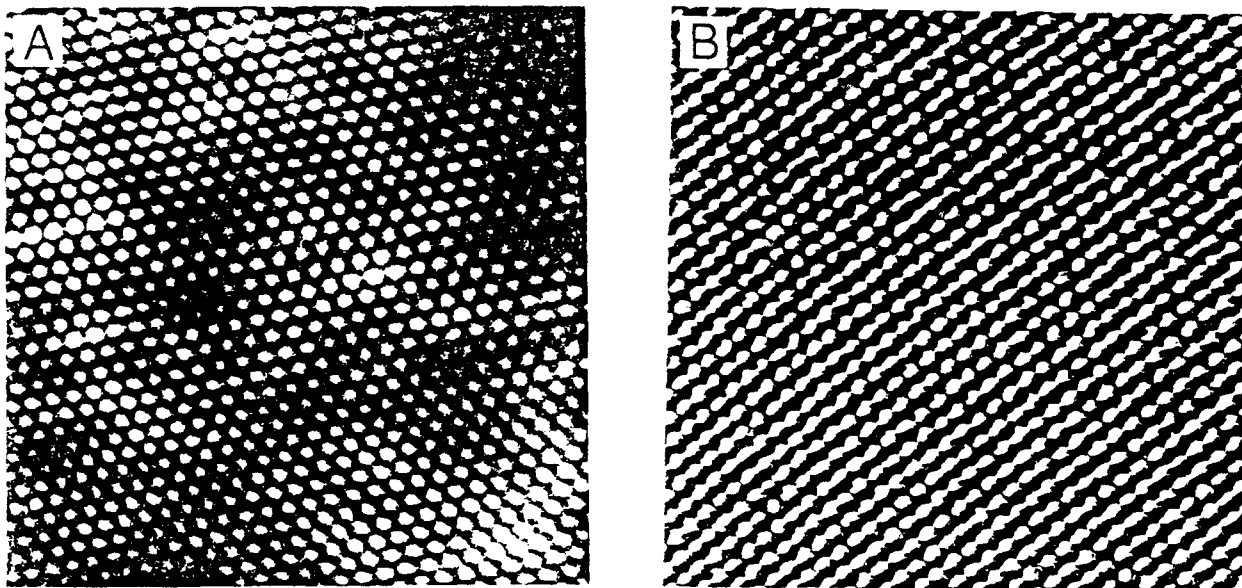


FIGURE 2-5. 9 nm x 9 nm (a) STM and (b) AFM images of  $\text{MoS}_{1.75}\text{Se}_{0.25}$ . The white scale bar corresponds to 0.9 nm.

In addition, the observed atomic corrugations in these STM and AFM images are similar to the corrugations determined from images of  $\text{MoS}_2$ . These STM and AFM experiments have thus shown that the structural and electronic properties of  $\text{MoS}_2$  are not perturbed significantly by Se-substitution. It is expected, therefore, that the coefficients of friction for  $\text{MoS}_{1.75}\text{Se}_{0.25}$  and  $\text{MoS}_2$  will be similar.

In contrast, we have discovered significant atomic level structural changes at the surfaces of Te-substituted  $\text{MoS}_2$ . Representative STM and AFM images are shown in Figure 2-6.

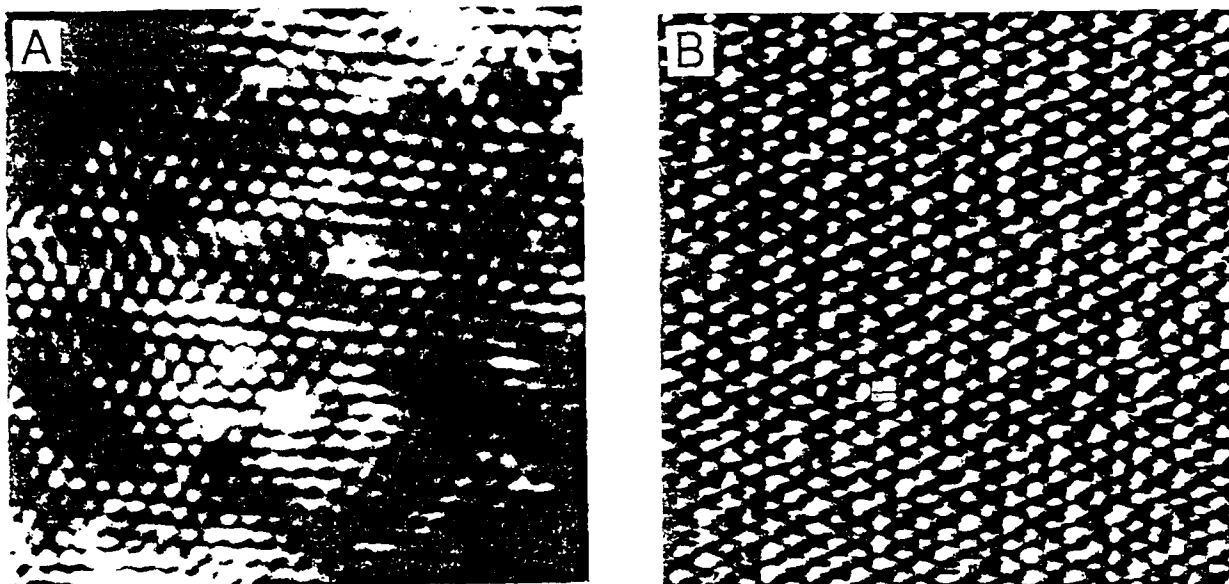


FIGURE 2-6 8 nm x 8 nm (a) STM and (b) AFM images of  $\text{MoS}_{1.75}\text{Te}_{0.25}$ . The small arrow in (b) highlights one local atomic protrusion.

The STM images exhibit hexagonal structure with a period and vertical corrugation similar to that determined for pure  $\text{MoS}_2$ . These results have shown that there are no large perturbations in the electronic states upon Te-substitution. The AFM images have shown, however, well-defined atomic size protrusions (Fig. 2-6 (b)). Since we have shown that the number of protrusions scales directly with the Te concentration it is likely that they correspond directly to the tellurium atoms in the lattice. Hence, it is possible that Te-substitution may reduce the layer-layer shear energy and corresponding sliding friction.

### Section-3

## REACTIVITY AND WEAR OF MoS<sub>2</sub> AND NbSe<sub>2</sub>

### 3.1 WEAR OF MoS<sub>2</sub> VERSUS NbSe<sub>2</sub>

The effective lubricating properties of quasi-two-dimensional materials such as MoS<sub>2</sub> is typically ascribed to facile interlayer shear of the van der Waals bonded layers.<sup>3,4</sup> However, factors other than this layered structural motif must also be important since structurally similar transition metal dichalcogenide materials are not all good lubricants. In the case of MoS<sub>2</sub> and NbSe<sub>2</sub>, the inferior properties of NbSe<sub>2</sub> have been attributed to the less facile interlayer shear that results from the different electronic configuration of Nb(IV) versus Mo(IV).<sup>4,5</sup> Direct support of this proposal and more generally a detailed microscopic understanding of friction and wear in these materials have, however, not been available. Using AFM we have been able to provide new and general data addressing the differences between these new materials.

AFM images recorded on freshly cleaved NbSe<sub>2</sub> crystal surfaces exhibit defects typically 7-10 nm wide at the surface and one layer deep ( $0.65 \pm 0.03$  nm). The density of defects is about  $7 \times 10^{-5}/\text{nm}^2$ . In contrast, freshly cleaved MoS<sub>2</sub> surfaces do not exhibit similar defects. Surprisingly, repetitive scanning of NbSe<sub>2</sub> and MoS<sub>2</sub> surface regions that contain defects has been shown to lead to dramatic wear and material removal. There are, however, several important differences in the details of wear on MoS<sub>2</sub> versus NbSe<sub>2</sub> (Fig. 3-1).<sup>22,29</sup>

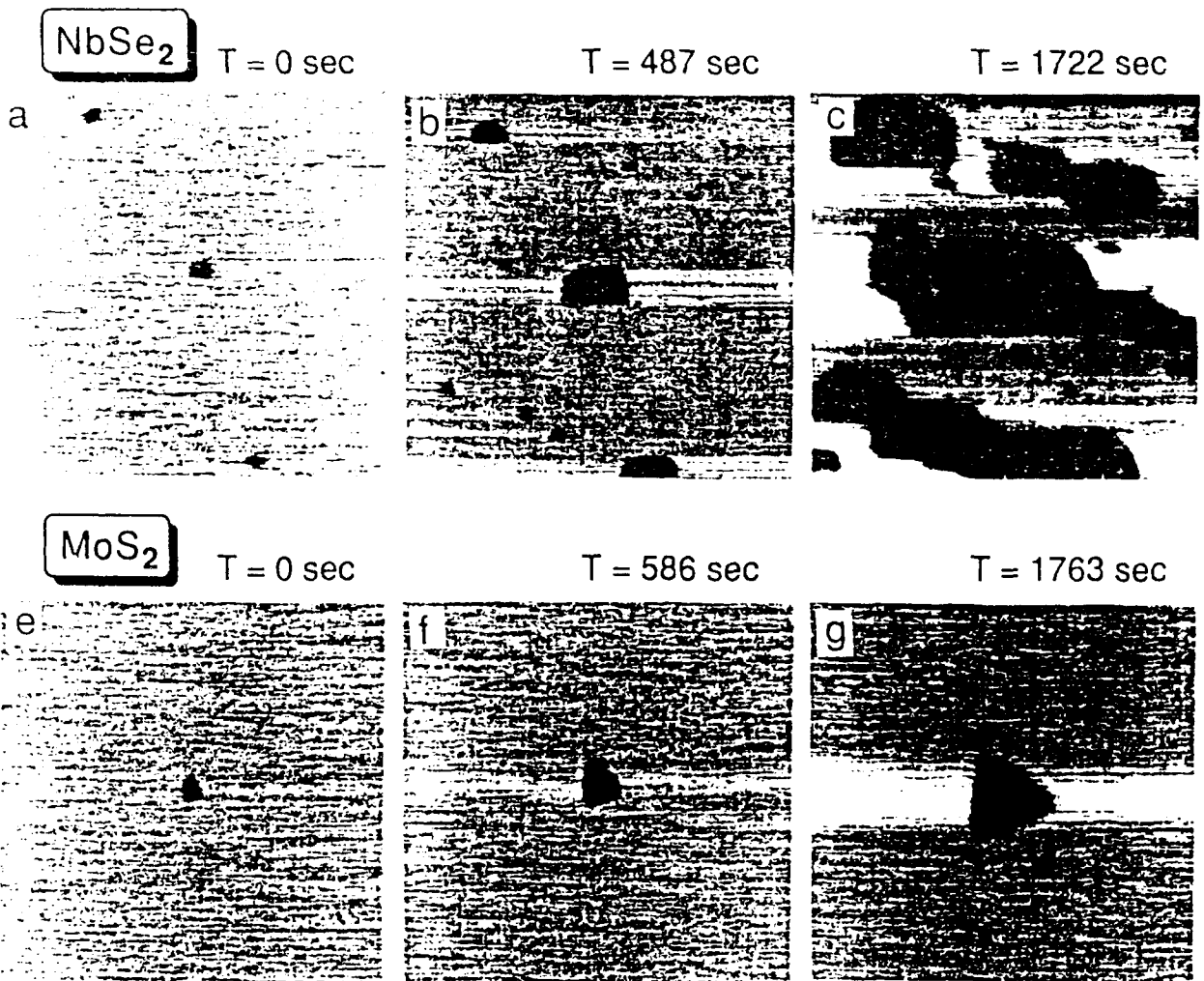


FIGURE 3-1. Time sequence of images recorded on NbSe<sub>2</sub> (upper panels) and MoS<sub>2</sub> (lower panels).

First, for similar imaging forces ( $10^{-8}$  -  $10^{-7}$  N) we have shown that it takes at least five times longer to wear a similar size area on MoS<sub>2</sub> versus NbSe<sub>2</sub>.<sup>29</sup>

Secondly, we have found that the initial defect on the MoS<sub>2</sub> surface grows preferentially in a triangular shape from a size of 10 to > 200 nm on edge. Atomic resolution images demonstrate that wear occurs preferentially along the three equivalent crystal lattice directions, and not along the scan direction as observed for NbSe<sub>2</sub>. The observations of

highly selective wear and a significantly lower wear rate for MoS<sub>2</sub> indicate that this surface is intrinsically more stable than that of NbSe<sub>2</sub>. Notably, previous studies addressing the tribological properties of MoS<sub>2</sub> and NbSe<sub>2</sub> did not consider the higher stability of MoS<sub>2</sub> to explain its superior properties. Our new studies have shown that the intrinsic stability of the MoS<sub>2</sub> interface must play an important role in the effectiveness of this lubricant.

### 3.2. OXIDATION OF MoS<sub>2</sub> and NbSe<sub>2</sub>

Since many technological applications of transition metal dichalcogenide lubricants require their use in oxidizing environments we have also characterized the microscopic details of oxidation for MoS<sub>2</sub> and NbSe<sub>2</sub>.

AFM measurements have provided unique insight into this problem, and furthermore, these data have also highlighted the distinct differences between MoS<sub>2</sub> and NbSe<sub>2</sub>. Oxidation of MoS<sub>2</sub> at 440°C was found to produce small defects in the MoS<sub>2</sub> surface as shown in Figure 3-2.

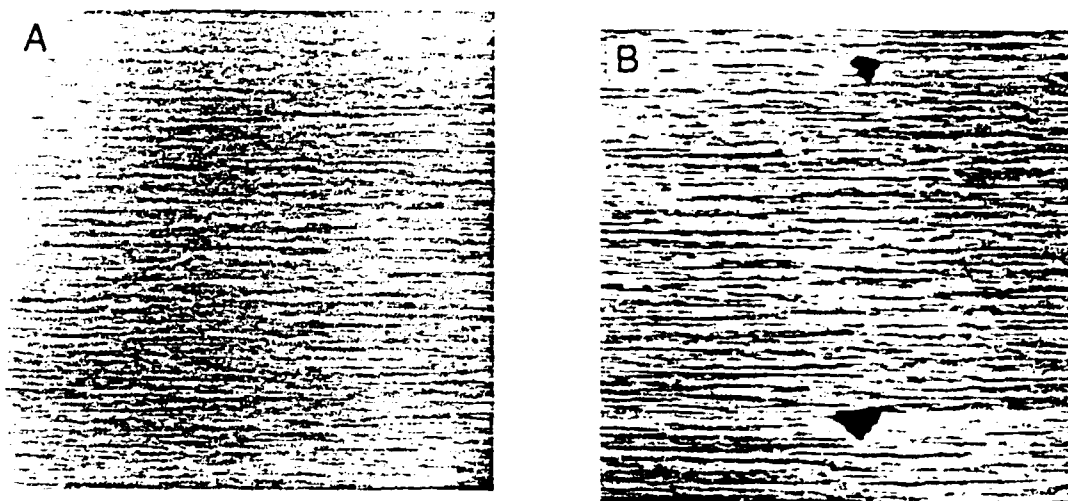


FIGURE 3-2. 660 x 660 nm<sup>2</sup>. AFM images of (a) MoS<sub>2</sub> and (b) oxidized MoS<sub>2</sub>. The crystal was oxidized in air at 440°C for five minutes.

The size and density of defects on MoS<sub>2</sub> following this oxidation are similar to that found on NbSe<sub>2</sub> at room-temperature. These results also indicate that MoS<sub>2</sub> is intrinsically more stable than NbSe<sub>2</sub>. Dramatic support of our hypothesis has come from oxidation studies of NbSe<sub>2</sub>. Specifically, oxidation of NbSe<sub>2</sub> at 220°C for five minutes in air causes extensive surface degradation as shown in Figure 3-3.

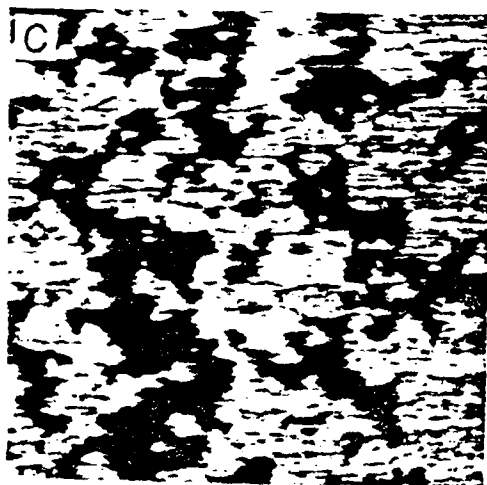


FIGURE 3-3. 660 x 660 nm<sup>2</sup> AFM image of NbSe<sub>2</sub> following oxidation in air at 220°C for five minutes.

The oxidation of NbSe<sub>2</sub> at temperatures  $\approx$  200°C less than used for MoS<sub>2</sub> causes oxide of large areas of the surface and deep defects and contrasts the small defects observed in the case of MoS<sub>2</sub>. These results have thus clearly shown that MoS<sub>2</sub> surfaces are more stable than NbSe<sub>2</sub> surfaces. Furthermore, since wear occurs preferentially at defects, the results from this project show that NbSe<sub>2</sub> would be a poor choice for a lubricant at elevated temperatures but MoS<sub>2</sub> may be acceptable.

The oxidation of MoS<sub>2</sub> was also investigated over a range of temperatures to investigate the stability range of this interface and the products formed by oxidation. AFM studies of MoS<sub>2</sub> oxidized at varying temperatures for fixed time periods have revealed

several new and important points. First, for oxidation temperatures  $\leq 420^\circ\text{C}$  no detectable defects are observed at the  $\text{MoS}_2$  interface (Fig. 3-4).

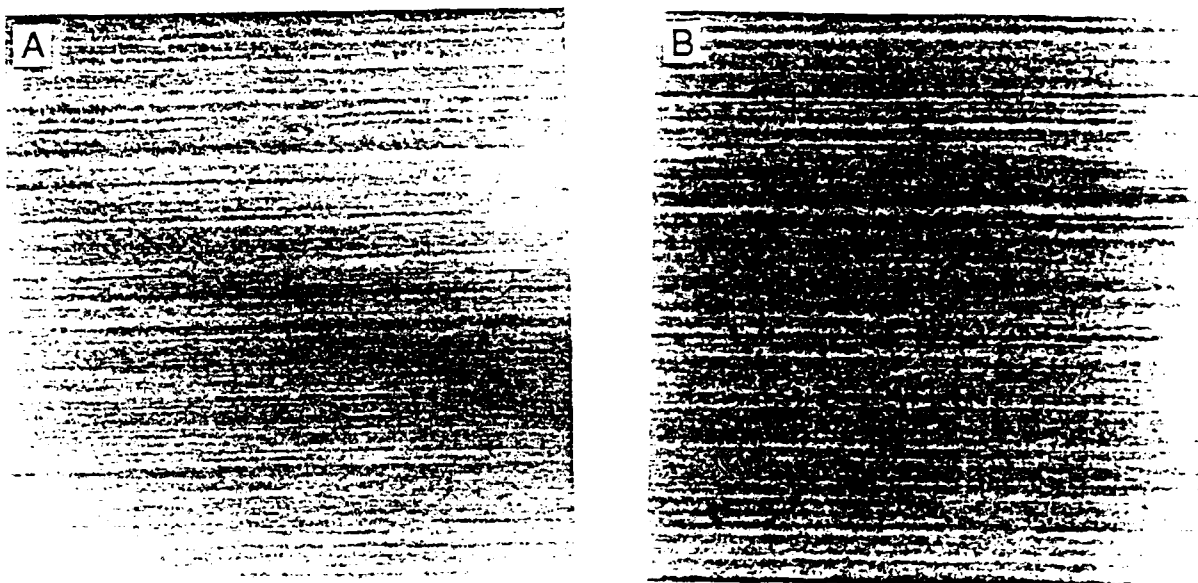


FIGURE 3-4.  $2 \times 2 \mu\text{m}^2$  AFM images recorded on  $\text{MoS}_2$  samples oxidized in  $\text{O}_2$  for five minutes at (A)  $400^\circ\text{C}$  and (B)  $420^\circ\text{C}$ .

Samples oxidized at  $> 420^\circ\text{C}$  show, however, defects and other surface features. Oxidation at  $440^\circ\text{C}$  for five minutes leads to the formation of trigonal pits  $20 \pm 5 \text{ nm}$  on edge and one S-Mo-S layer deep. the average density of these defects is  $1.1 \times 10^{-6}/\text{nm}^2$ . As the oxidation temperature was increased we found that the defect density increased only slightly, however, the size of the defects increased significantly as shown in Figure 3-5.

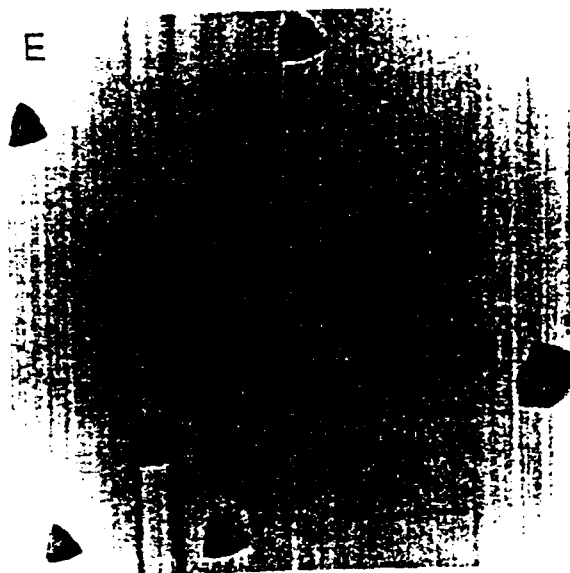
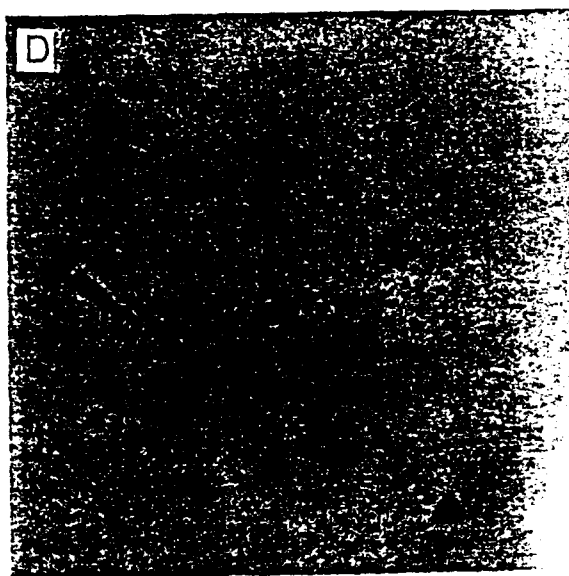
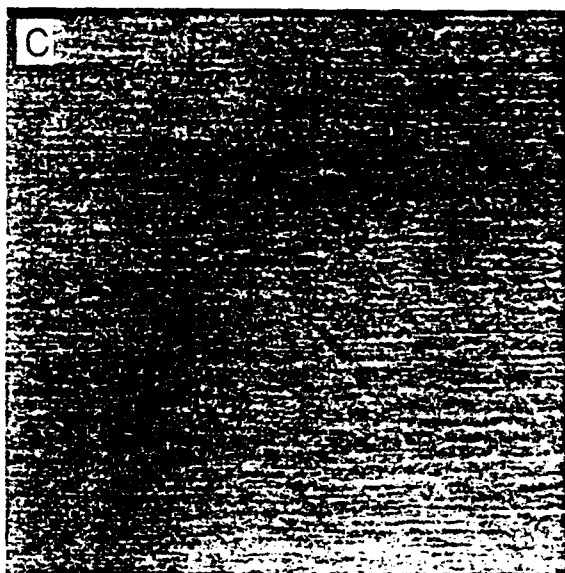


FIGURE 3-5. 2 μm x 2μm AFM images recorded on MoS<sub>2</sub> samples that were oxidized in O<sub>2</sub> for five minutes at (C) 440°C, (D) 460°C and (E) 480°C.

After oxidation at 460°C the triangular defects had increased in size to approximately 100 nm on edge and after the 480°C oxidation these defects further increased in size to  $210 \pm 30$  nm.

In addition, we have also discovered the growth of crystallites on the surface of MoS<sub>2</sub> following oxidation at temperatures  $\geq 480^{\circ}\text{C}$ . The size of the crystallites, which appear as light plates in images, increases with increasing oxidation time and/or temperature as shown in Figure 3-6.

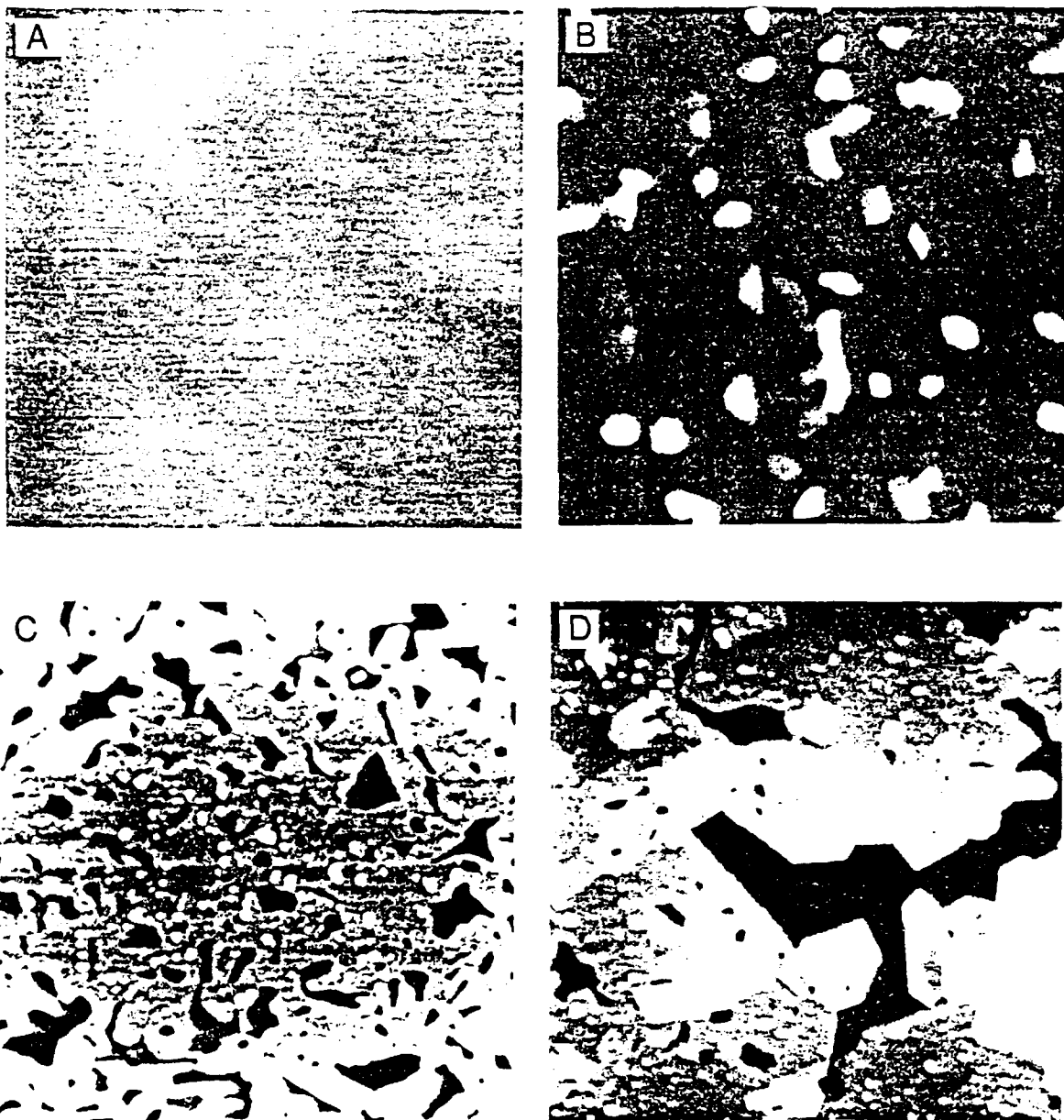


FIGURE 3-6.  $3\ \mu\text{m} \times 3\ \mu\text{m}$  AFM images recorded on MoS<sub>2</sub> samples that were oxidized at  $480\ ^{\circ}\text{C}$  for (A) 2, (B) 5, (C) 8 and (D) 11 minutes.

Analysis of the crystal surfaces (following oxidation) by X-ray photoelectron spectroscopy (XPS) has shown that the new features detected in the AFM images correspond to the Mo(VI) oxide, MoO<sub>3</sub>. Hence, we have shown that oxidation of MoS<sub>2</sub> initially proceeds ( $T \geq 440^\circ\text{C}$ ) with the formation of small defects, which probably function as nucleation sites, and then growth of micron size crystallites of MoO<sub>3</sub>. This process is shown schematically in Figure 3-7.

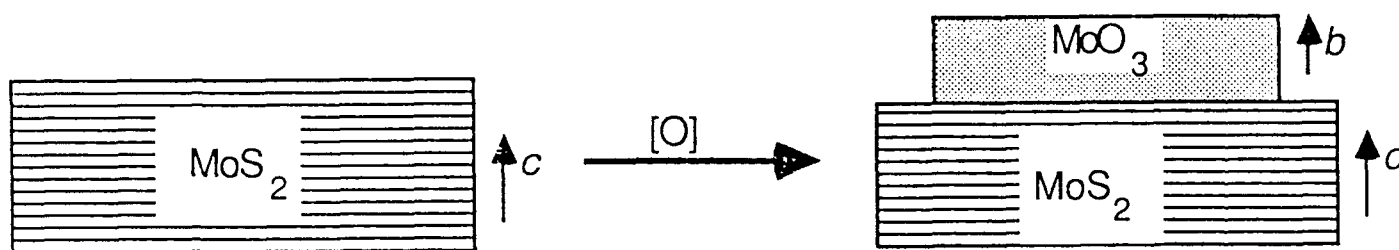


FIGURE 3-7. Schematic view of MoS<sub>2</sub> before and after oxidation, [O]. The MoO<sub>3</sub> crystallite grows with its b-axis perpendicular to the MoS<sub>2</sub> surface.

### 3.3 WEAR AND NANOFABRICATION

Since it is reasonable to expect that MoO<sub>3</sub> also form an MoS<sub>2</sub> in applications environments we also characterized its tribological properties with the AFM. In general, we have found that both the MoO<sub>3</sub> and MoS<sub>2</sub> surfaces are stable to repetitive scanning when the imaging force is  $\leq 10^{-8}$  N. When the imaging force is increased to  $\geq 5 \times 10^{-8}$ , however, the MoO<sub>3</sub> surface (but not MoS<sub>2</sub>) exhibits wear. We have exploited this wear process as a means to nano-machine MoO<sub>3</sub> in a controlled manner with high resolution.<sup>23,27,30</sup>

For example, a line 150 nm long is shown in Figure 3-8. The width of the lines in this figure are only 10 nm at the MoO<sub>3</sub> and decrease to 5 nm at the MoO<sub>3</sub>/MoS<sub>2</sub> interface. The average aspect ratio is thus on the order of 20:1, and it has been possible to create structures with aspect ratios as high as 40:1. Such high-resolution line structures may have application as diffraction gratings.

In addition to simple linear features, we have also used the nanomachining process to create significantly more complex structures (Figure 3-8).

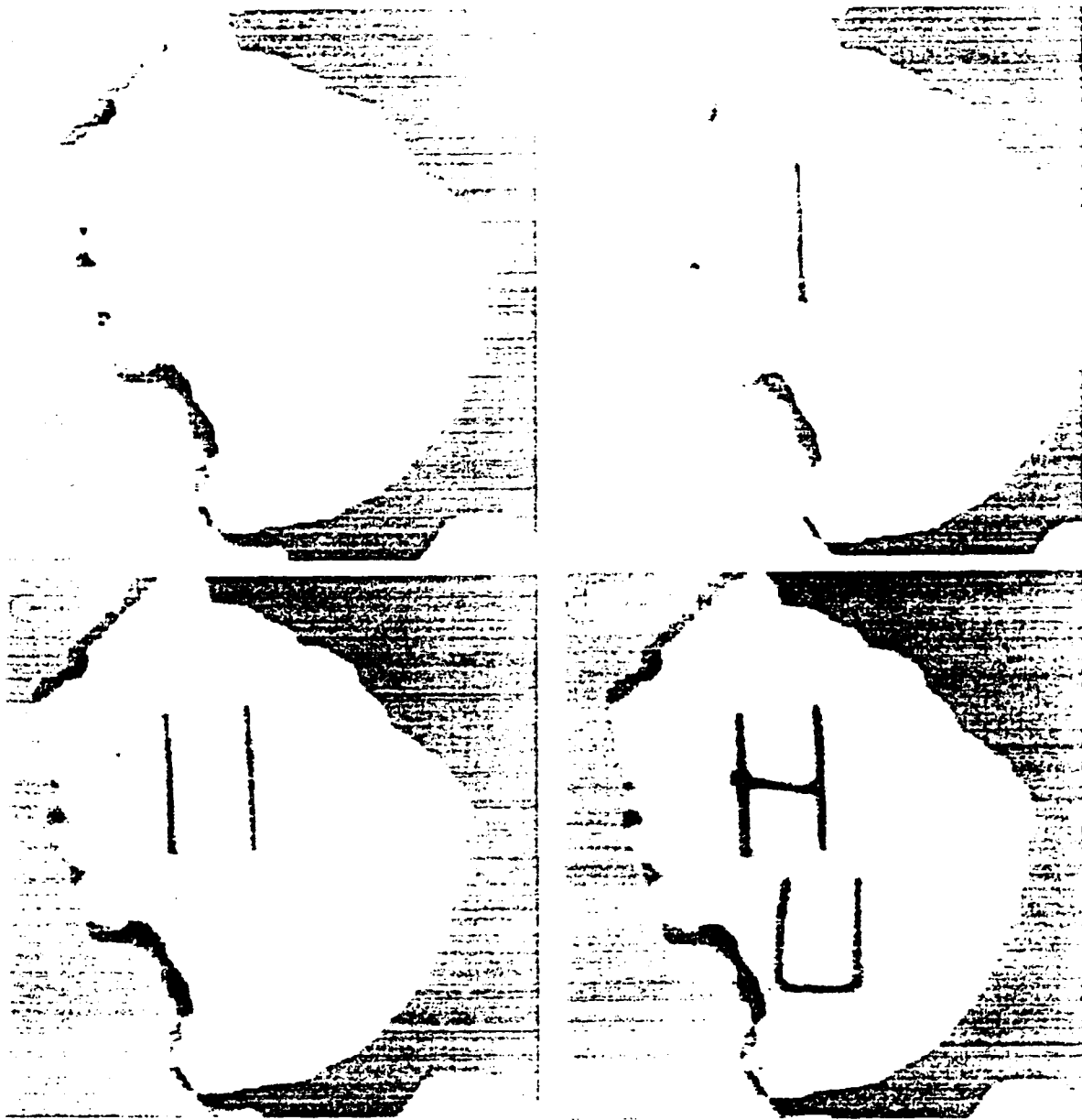


FIGURE 3-8. Series of  $500 \times 500 \text{ nm}^2$  AFM images showing the machining of the pattern "HU". The images were recorded nondestructively using an applied load of  $1 \times 10^{-8} \text{ N}$ ; nanomachining was carried out using forces  $\geq 5 \times 10^{-8} \text{ N}$ .

We have illustrated this point by creating the pattern "HU".<sup>23,27</sup> It is important to note that the nanomachining resolution does not degrade during these operations, and thus it will be possible to use or follow procedures designed to create structures with a resolution which exceeds that obtainable by conventional lithography.

We have also used AFM for the controlled manipulation of nanostructures.<sup>23,27,30</sup> The underlying basis for structure manipulation in the MoO<sub>3</sub>/MoS<sub>2</sub> system is that MoO<sub>3</sub> is not strongly bound to the MoS<sub>2</sub> substrate. It is thus possible to pattern a structure in MoO<sub>3</sub>, separate this structure from the MoS<sub>2</sub> substrate, and then manipulate the object on the MoS<sub>2</sub> surface. This process is illustrated in Figure 3-9 for a triangular object approximately 80 nm on edge.

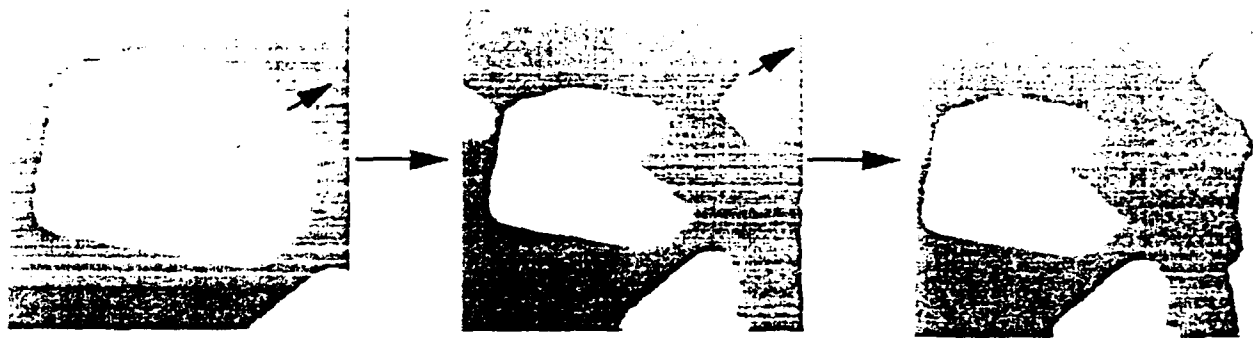


FIGURE 3-9. Series of AFM images exhibiting the manipulation of a triangular MoO<sub>3</sub> object on the MoS<sub>2</sub> surface. The two translations shown in (b) and (c) each correspond to a distance of  $\approx 100$  nm.

It is possible to move objects using large forces ( $\approx 10^{-7}$  N) and image the resulting manipulations without further perturbation using a small force. Hence, we have demonstrated that it is possible to monitor manipulation processes in-situ, thus enabling exquisite control and precise positioning of objects and structures.

## Section-4

### METAL-SUBSTITUTED TANTALUM DISULFIDE

#### 4.1 INTRODUCTION

A general and fundamental goal of our studies has been to understand from a microscopic perspective how dopants affect the properties of solids. To this end we have also investigated metal-substitution in other solids, and in particular, tantalum disulfide.<sup>9-20</sup> The emphasis in this work has been to probe how these metal-dopants interact with the charge density wave in this material.

Understanding the nature of the interaction between impurities and a charge density wave (CDW) is essential to understanding the static and dynamic properties of the CDW state.<sup>31-32</sup> In general, pinning can be defined as either strong or weak depending on the competing energetics of the CDW-impurity interaction and the CDW deformation energy.<sup>32</sup> In strong pinning the impurity potential dominates the CDW elastic energy and pins the phase of the CDW at each impurity site. In weak pinning the CDW breaks up into constant phase regions that are pinned collectively by impurities. Despite the fundamentally different structural manifestations of strong and weak pinning, there has been considerable controversy concerning the nature of pinning in CDW systems.<sup>20,24,33-35</sup> This controversy has been due in large part to the lack of direct data characterizing the evolution of CDW structure with impurity doping. Real-space imaging of the CDW structure in doped materials by scanning tunneling microscopy (STM) is, however, beginning to provide a direct method of addressing the essential issue of strong versus weak pinning.<sup>20-24</sup>

In addition, an important and general consequence of pinning is structural disorder. In two-dimensional (2D) systems disorder can manifest itself in intriguing ways. For example, Halperin and Nelson predicted that a 2D solid can melt in a continuous transition through a hexatic state that is characterized by long-range orientational order and exponentially decaying positional order.<sup>36</sup> This unique hexatic state arises from the formation of

topological defects, dislocations, in the lattice. Disorder due to impurity pinning has many similarities to melting, although the melting theory is based upon equilibrium thermal disorder whereas pinning is typically a quenched disorder. Since statistical averaging differs for equilibrium and quenched disorder<sup>37</sup> it is important to examine carefully the analogy of disorder in pinned systems to equilibrium theory.

We have addressed the nature of CDW impurity pinning in Nb-doped TaS<sub>2</sub>, Nb<sub>x</sub>Ta<sub>1-x</sub>S<sub>2</sub>, and have elucidated the detailed characteristics of disorder in this pinned CDW system. Real-space images of the CDW lattice as a function of Nb impurity concentration were obtained by STM, and were quantitatively analyzed to determine the topological defects and the radial, translational and orientational correlation functions. These data show unambiguously that CDW pinning by the Nb impurities is weak or collective. In addition, our work demonstrates that this system evolves through crystalline, hexatic glass and amorphous states as a function of impurity concentration.

#### 4.2 STM CHARACTERIZATION

High resolution STM images of the Nb<sub>x</sub>Ta<sub>1-x</sub>S<sub>2</sub> materials are shown in Figures 4-1 to 4-3. Images of the incommensurate CDW phase of undoped TaS<sub>2</sub> samples exhibit a well-ordered hexagonal CDW superlattice and atomic lattice (Fig. 4-1).

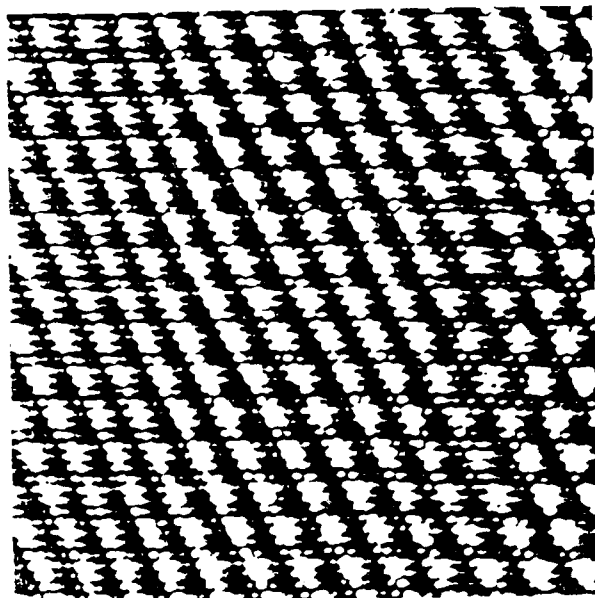


FIGURE 4-1. STM image of a TaS<sub>2</sub> recorded at 360 K. The image exhibits both the atomic lattice ( $a = 3.35 \text{ \AA}$ ) and CDW super lattice ( $a = 11.8 \text{ \AA}$ ).

In contrast, substitution of Nb causes disorder in the CDW lattice (Figs. 4-2, 4-3). The images of the  $x(\text{Nb}) = 0.02$  samples exhibit areas in which the CDW lattice has hexagonal order, and also regions containing defects; these defects introduce disorder into the CDW lattice.



FIGURE 4-2. STM images of the incommensurate CDW state in (a)  $\text{Nb}_{0.02}\text{Ta}_{0.98}\text{S}_2$  and (b)  $\text{Nb}_{0.04}\text{Ta}_{0.96}\text{S}_2$ . Black lines highlight the insertion of an extra row of CDW lattice sites in (a). Two distinct loops and Burgers vectors are drawn in (b) to highlight dislocations in the CDW lattice. A 5-fold-7-fold disclination pair is also shown in (b).

The predominant defects observed in the samples containing  $x(\text{Nb}) \leq 0.04$  are dislocations. Dislocations are formed by the insertion of an extra half row of CDW sites in the lattice; black lines in Figure 4-2 highlight the creation of one dislocation. An important point to recognize about these defects is that there is a significant strain field at the dislocation.<sup>38</sup> The CDW can relax the strain field by locally deforming (i.e., rotating), although such local rotations create disorder.

As the impurity concentration increases to  $x(\text{Nb}) = 0.04$  we find that dislocations appear with a higher density than in the  $x(\text{Nb}) = 0.02$  samples (Fig. 4-2b). The CDW lattice rows near the dislocation are deformed as discussed above. However, in areas free of dislocations the CDW lattice is locally ordered. We have highlighted several dislocation cores (the region where the CDW deforms) by constructing Burgers loops (Fig. 4-2b). The Burgers loop consists of an equal number of steps along each lattice direction; the loop will remain open if it encloses a single dislocation. The vector pointing from start to end of the loop, the Burgers vector, uniquely defines the dislocation.<sup>38</sup> We find that the Burgers vectors defining the CDW dislocations in the Nb-doped samples occur along each of the three crystallographic axes, and thus we conclude that impurity-induced dislocations occur randomly in the CDW lattice. In the samples containing higher impurity concentrations,  $x(\text{Nb}) = 0.07$  and  $0.10$  the STM images exhibit extended defects (Fig. 4-3).

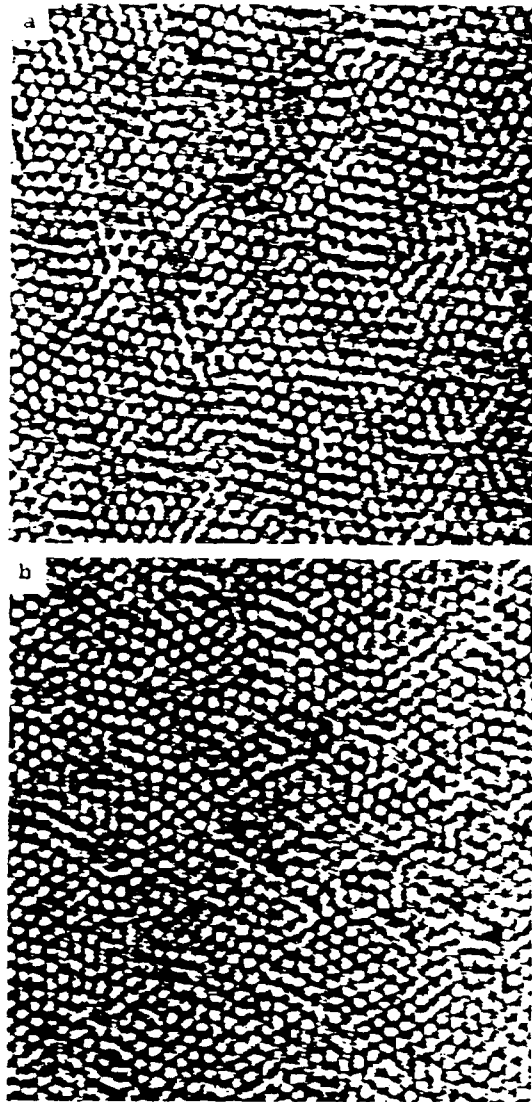


FIGURE 4-3. STM images of the incommensurate CDW phase in (a)  $\text{Nb}_{0.07}\text{Ta}_{0.93}\text{S}_2$  and (b)  $\text{Nb}_{0.1}\text{Ta}_{0.9}\text{S}_2$ .

The CDW lattice in these latter samples exhibit significant disorder with regions of hexagonal order extending only several lattice constants.

To elucidate in detail the topology and density of these defects we have quantitatively analyzed the STM images. The quantitative analysis involves defining the  $x,y$  coordinates of each CDW maxima and the unique nearest neighbors in the lattice. The CDW maxima,

which we call lattice sites, were located to  $\pm 1$  pixel accuracy by a thresholding algorithm. Once the lattice points are located, a sweepline algorithm is used to construct the Voronoi diagram for the lattice. The Voronoi diagram determines the nearest neighbors of all of the lattice points uniquely,<sup>39</sup> and thus can be used to illustrate explicitly all topological defects in the lattice. To illustrate these defects we triangulate the Voronoi diagram by drawing "bonds" from all CDW lattice points to their nearest neighbors. Hence, fully coordinated lattice sites are indicated by six bonds to the CDW maxima, while defects contain fewer or greater bonds. Typical results obtained from the analysis of  $x(\text{Nb}) = 0, 0.02, 0.04, 0.07$  and  $0.10$  samples are shown in Figure 4-4.

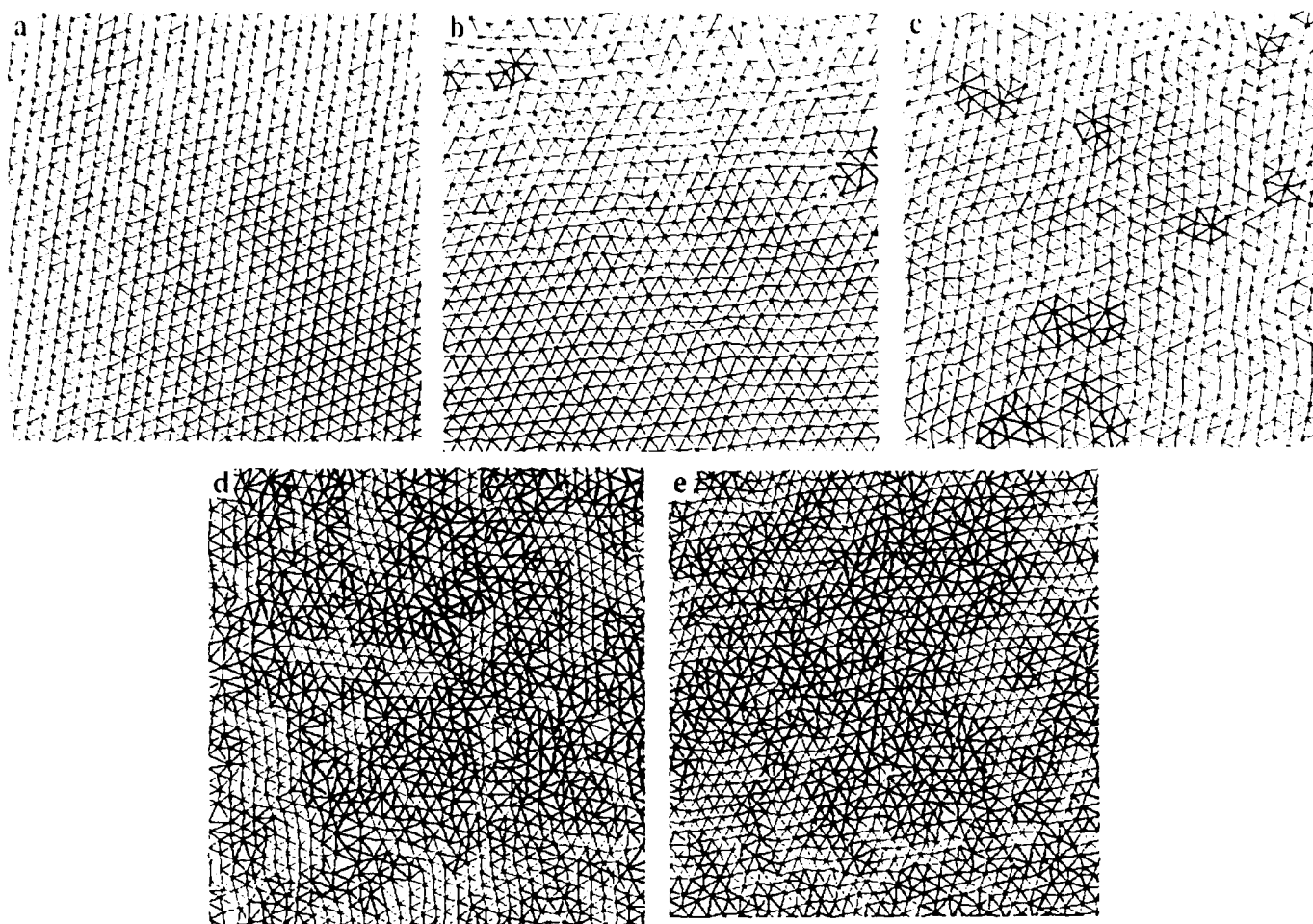


FIGURE 4-4. Triangulations of the STM images recorded on  $\text{Nb}_x\text{Ta}_{1-x}\text{S}_2$  crystals where (a)  $x = 0$ , (b)  $x = 0.02$ , (c)  $x = 0.04$ , (d)  $x = 0.07$ , and (e)  $x = 0.10$ . Lattice sites that do not have six-fold coordination are highlighted by shading the triangles which have the non-six fold coordinate site as a vertex.

In these triangulations we have highlighted the defect (non-six-fold coordinate) sites by shading. Analyses of images recorded on pure  $\text{TaS}_2$  show that the CDW lattice is free of topological defects; that is, all of the lattice sites are sixfold coordinate (Fig. 4-4a). The triangulations explicitly show, however, that the Nb-doped materials have topological defects in the CDW lattice. At low concentrations of impurities,  $x(\text{Nb}) = 0.02$  and  $0.04$ , we find that the dislocations consist of fivefold/sevenfold disclination pairs (Fig. 4-4). Extended defect

networks are also obvious in the triangulation data for the  $x(\text{Nb}) = 0.07$  and  $0.10$  samples. These extended topological defects consist of dislocations and free disclinations.

We have also used this data to determine the separation between dislocations. We find that the average spacing between dislocations in the  $x(\text{Nb}) = 0.02, 0.04, 0.07$  and  $0.1$  CDW lattices is 12, 8, 5, 3 lattice constants, respectively. In comparison, the average separation between the Nb impurities in the lattice ( $d_i$ ) is 0.80, 0.57, 0.43 and 0.36 CDW lattice constants, respectively. The average separation between dislocations is thus always greater than the average impurity spacing; that is, impurity pinning of the CDW must be a collective effect. Hence, these results show that CDW pinning in the  $\text{Nb}_x\text{Ta}_{1-x}\text{S}_2$  materials is weak.

#### 4.3 THEORETICAL ANALYSIS

To further examine the issue of CDW pinning we consider theoretical models of the CDW-impurity interaction. The one-dimensional model first proposed by Fukuyama, Lee and Rice (FLR) has been the most widely studied example for CDW-impurity pinning.<sup>32</sup> For this one-dimensional model the CDW wave function is

$$\rho(x) = \rho_0 + \rho \cos(Q \cdot x + \phi(x)) \quad (1)$$

where  $\rho(x)$  is modulated charge density,  $\rho_0$  is the background charge density,  $\rho$  is the CDW amplitude,  $Q$  is the CDW wave vector, and  $\phi(x)$  is CDW phase. Analysis of this model shows that there are two distinct regimes which describe the strength of the CDW-impurity interaction (i.e., strong and weak pinning). These two regimes can be defined in terms of a competition between the pinning energy  $E_p = V_0\rho$  and the CDW elastic energy  $E_e = \alpha\kappa$ . In strong pinning the impurity potential  $V_0$  dominates the elastic energy:  $\epsilon = V_0\rho/\alpha\kappa \gg 1$ . Since the CDW is pinned to each impurity site in the lattice the CDW phase undergoes abrupt changes at the impurity sites. Conversely, in weak pinning the CDW stiffness resists deformation by the impurity potential:  $\epsilon \ll 1$ . For weak pinning the total energy is minimized through collective interactions. Hence, the CDW phase can vary smoothly over a region containing many impurities.

The 2D CDW system studied here should form areas with local phase coherence and positional order if the system is weakly pinned. Dislocations and other defects will separate phase coherent regions. These locally coherent regions can be understood by scaling arguments. For an area of length scale  $L$  with impurity density  $n_i$ , the energy gain from pinning per unit area will be  $V_0\rho(L^2n_i)^{1/2}L^{-2}$  while the elastic energy cost is  $\sim\alpha\kappa L^{-2}$ .<sup>40</sup> By minimizing the total energy density one finds an optimized correlation length  $L_c$ ,

$$L_c = (2/\epsilon)d_i \quad (2)$$

Where  $d_i=(1/n_i)^{1/2}$  is the spacing between impurities. Within the length scale  $L_c$ , the CDW phase varies smoothly between  $-\pi$  and  $\pi$ ; positional correlations will only be sustained on a scale smaller than  $L_c$ . Alternatively, this scaling argument can be used to explain the formation of dislocations. The energy cost for a dislocation loop with size  $L$  is  $\sim\alpha\kappa$  up to a logarithm,<sup>38</sup> while the energy gain due to pinning is  $V_0\rho(L^2n_i)^{1/2}$ . Hence, creating a dislocation on length scale larger than  $L_c=(2/\epsilon)d_i$  is energetically favorable.

As discussed above the spacing between dislocations in the CDW lattice is significantly larger than the distance between Nb impurities.<sup>24</sup> This observation is consistent with the weak pinning model developed above. A related criteria for weak-pinning is the presence of ordered regions with a critical size directly proportional to the impurity spacing. Notably, analysis of large area STM images demonstrate that areas of the CDW lattice that are free from dislocations exhibit a smooth variation in the CDW phase as we expect for the case of weak pinning. Moreover, we can use our scaling equation to estimate the magnitude of the dimensionless parameter  $\epsilon$ . Using the  $L_c$  determined from our images and the known impurity spacing we find that  $\epsilon = 0.1-0.2 \ll 1$ . These results demonstrate convincingly that the CDW pinning in  $Nb_xTa_{1-x}S_2$  is weak.

It is also important to examine the consequences of the disorder produce by weak pinning in this system. We first examine the structure factor,  $S(k) = |\rho(k)|^2$ , to investigate the average structural effects of pinning.  $S(k)$ 's were calculated from the square of the Fourier

transform of the STM images; the results for the  $x(\text{Nb}) = 0.02, 0.04, 0.07$  and  $0.10$  samples are shown in Figure 4-5.

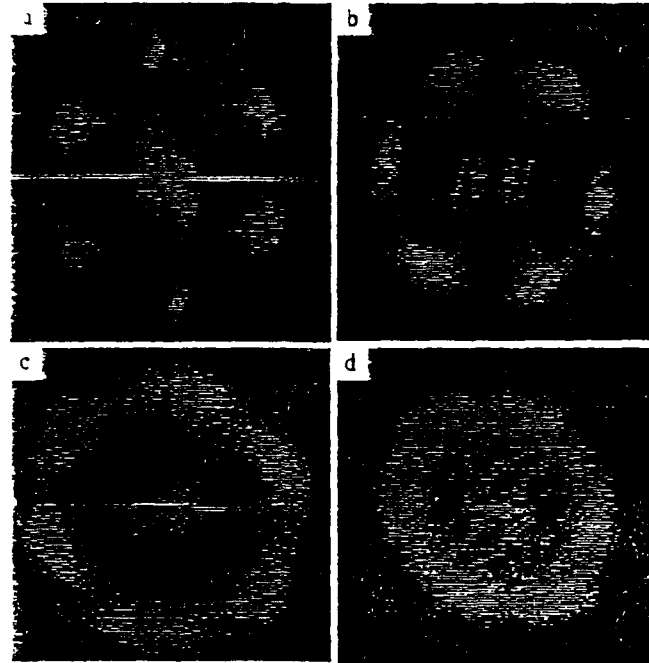


FIGURE 4.5 Structure factors corresponding to the CDW lattices of (a)  $x = 0.02$ , (b)  $x = 0.04$ , (c)  $x = 0.07$ , and (d)  $x = 0.10$   $\text{Nb}_x\text{Ta}_{1-x}\text{S}_2$  materials.

$S(k)$  for pure  $\text{TaS}_2$  (not shown) exhibits sharp sixfold symmetric peaks. These peaks broaden both radially and angularly as the impurity concentration increases to  $0.04$ . For the  $x(\text{Nb}) = 0.07$  and  $0.10$  the first order Bragg peaks have broadened to form a ring whose intensity has a sixfold modulation. The angular broadening is due to CDW rotations that were discussed above in section A. This broadening indicates a loss of orientational order; however, it is not possible to provide a quantitative measure of the orientational disorder from this  $S(k)$  data. In addition, the radial widths of the Bragg peaks indicate that the translational correlation length is short in all of the Nb-doped materials. Notably, these  $S(k)$  data are qualitatively similar to the results expected for 2D melting through a hexatic state.<sup>36</sup>

To provide a quantitative measure of the order in this system and how it is affected by impurity pinning we have investigated the radial distribution, translational correlation and orientational correlation functions. The radial distribution function is defined as  $g(r) = \langle n(r) \rangle / N_0$ , where  $n(r)$  is the point density at distance  $r$  from the origin of the structure and  $N_0$  is the average density of points. For a general structure,  $g(r)$  tends to 1 as  $r \rightarrow \infty$ ; that is, the distribution of points at large distances appears uniform. The results of the calculations of  $g(r)$  are presented in Figure 4-6.

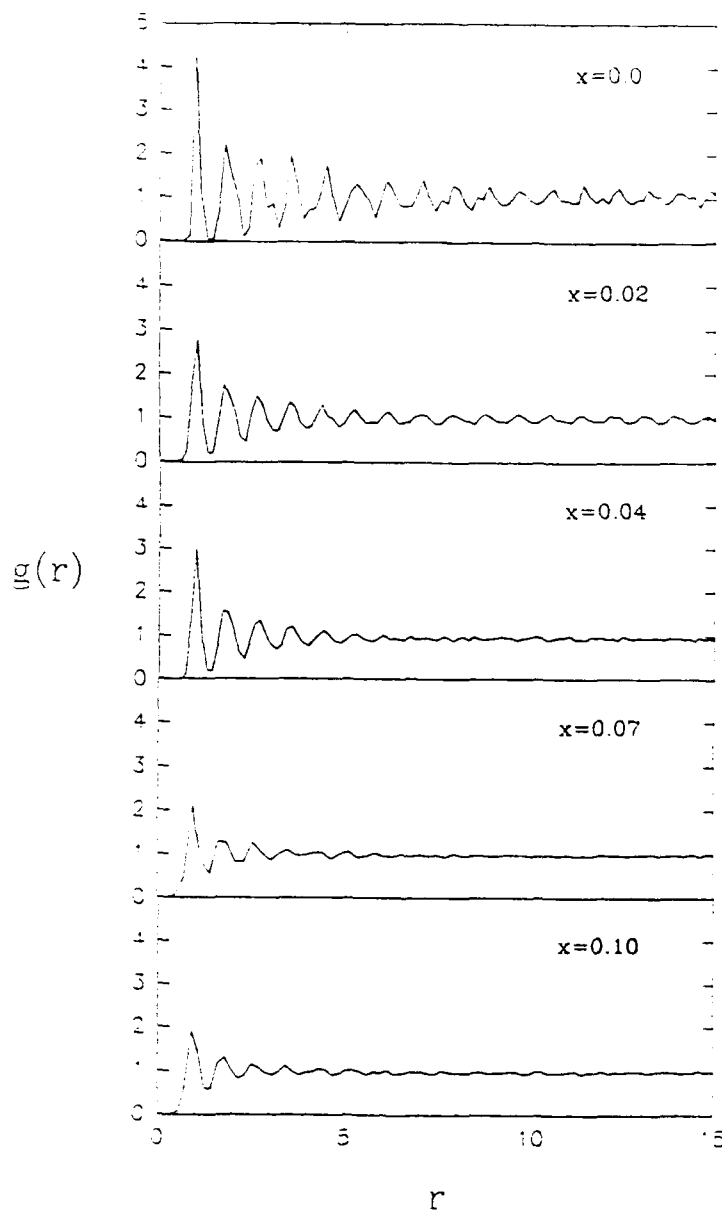


FIGURE 4-6. Radial distribution functions for the  $x = 0, x = 0.02, x = 0.04, x = 0.07,$  and  $x = 0.10$   $\text{Nb}_x\text{Ta}_{1-x}\text{S}_2$  materials. The x axis corresponds to CDW lattice constants.

For the  $x(\text{Nb}) = 0$  sample  $g(r)$  oscillates strongly out to more than 10 lattice constants. The persistent oscillation in  $g(r)$  indicates that positional order is long range. When the impurity level increases to 0.02 and 0.04 the amplitude of the oscillations in  $g(r)$  decreases and the

oscillations die out much more rapidly than in  $g(r)$  for the pure material. For the  $x(\text{Nb}) = 0.07$  or 0.1 materials the amplitude of the peaks in  $g(r)$  is further reduced and these peaks only persist to the second or third nearest neighbors. These results indicate that Nb impurities destroy translational order in this CDW system.

To further characterize the order of this 2D system we have calculated the translational and orientational correlation functions. Previous theoretical work has shown that these functions provide a unique description of the order in 2D systems.<sup>36</sup> The translational correlation function is defined as  $G_T(\vec{r}) = \langle \psi(0)\psi(\vec{r})^* \rangle$ , where  $\psi(\vec{r})$  is the translational order parameter at position  $r$ :  $\psi(\vec{r}) = \sum_{i=1}^3 \exp(i\vec{G}_i \cdot \vec{r}) / 3$ . The summation is over the three reciprocal lattice vectors,  $G_L$ . The orientational correlation function is  $G_6(\vec{r}) = \langle \psi_6(0)\psi_6(\vec{r})^* \rangle$ , where  $\psi_6(\vec{r})$  is the orientational order parameter:  $\psi_6 = \sum_{i=1}^{N_i} \exp(i6\theta(\vec{r})) / N_i$ .  $\theta(\vec{r})$  is the bond angle with respect to a fixed direction, where the "bonds" are the lines that connect nearest neighbors as in the triangulation (Fig. 4).  $N_i$  is the number of bonds at the  $i^{\text{th}}$  point and the summation is over all bonds at position  $r$ . For a perfect lattice  $G_T(\vec{r}) = G_6(\vec{r}) = 1$ .

Dislocations observed in the CDW lattice will reduce both  $G_T(\vec{r})$  and  $G_6(\vec{r})$ , although the detailed effect on these functions is expected to be quite different. Qualitatively, a dislocation is very effective in destroying translational order since it displaces the CDW sites on the order of one lattice constant. Translational order should, therefore, only be sustained in regions free of dislocations. Indeed, Halperin and Nelson showed that when the structural order is dominated by dislocations the translational correlation length  $\approx$  the dislocation spacing. In the case of  $G_6(\vec{r})$  the effect of dislocations is expected to be quite different. For a dislocation consisting of a bound pair of fivefold-sevenfold disclinations (Fig. 4), the bond orientational order parameters at these two points are obviously reduced. Because the disclinations are closely bound, they do not change the coordination number and orientation of points away from the dislocation. Hence, dislocations do not necessarily destroy orientational order.

The calculated results for  $G_T(\bar{r})$  and  $G_6(\bar{r})$  are shown in Figure 4-7.

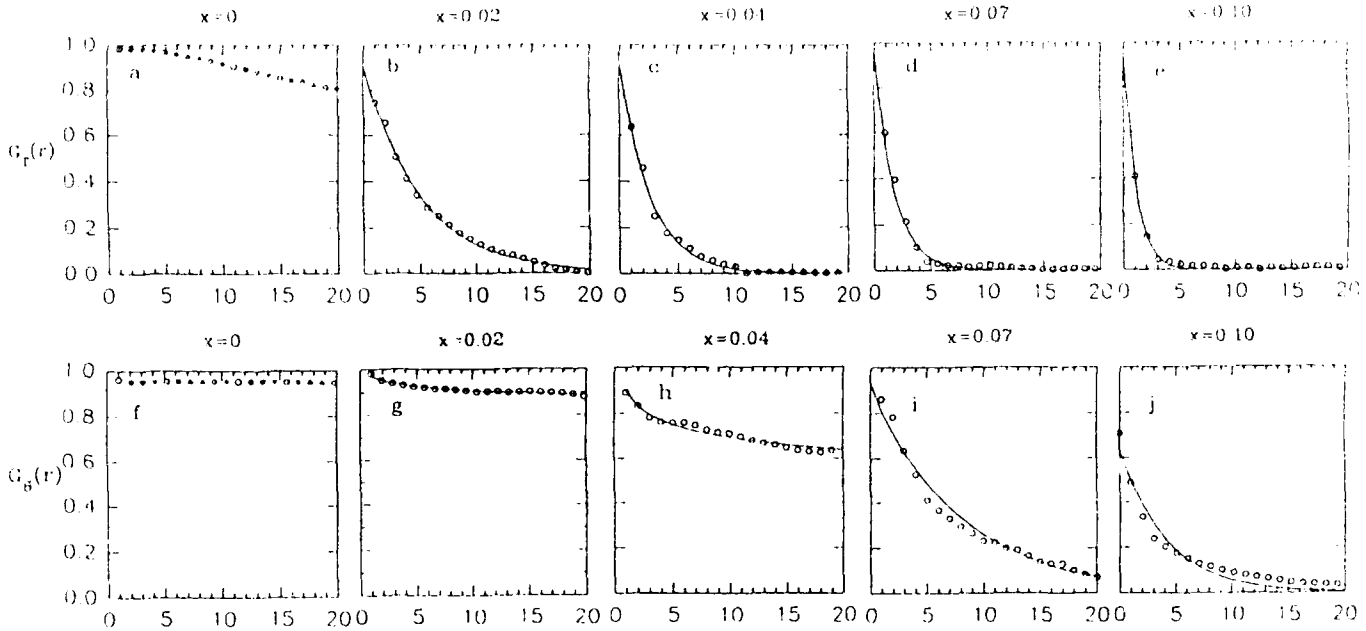


FIGURE 4-7. Translational correlation functions  $G_T(r)$  (a-e) and orientational correlation functions  $G_6(r)$  (f-j) calculated from images  $x = 0, 0.02, 0.04, 0.07,$  and  $0.10$   $Nb_xTa_{1-x}S_2$  materials. The  $x$  axes in these figures correspond to lattice constants. The points represent the experimental data, and the lines correspond to exponential ( $e^{-r/\xi}$ ) fits (a-e) and (i, j) or power law ( $r^{-1}$ ) fits (g, h).

$G_T(\bar{r})$  and  $G_6(\bar{r})$  decay very little over 20 lattice constants for the pure sample. However, all of the samples that contain Nb impurities exhibit a rapid decay of translational order. This decay in  $G_T(\bar{r})$  can be fit reasonably well to an exponential of the form  $G_T(\bar{r}) = \exp(-\xi_T/r)$ , where  $\xi_T$  is the translational correlation length. The range of the  $\xi_T$ 's determined by averaging a number of images are  $\xi_T = 7-10, 3-6, 2-3,$  and  $1-2$  lattice constants for the  $x(\text{Nb}) = 0.02, 0.04, 0.04,$  and  $0.10$  samples, respectively. The values of  $\xi_T$  are similar to the average

dislocation spacing determined from triangulation data (e.g., Fig. 4-2), and furthermore these results demonstrate quantitatively that weak pinning by the Nb impurities destroys translational order. In contrast, we find that the orientational correlations die out slowly for the 0.02 and 0.04 samples, although  $G_6(\vec{r})$  decays rapidly for  $x(\text{Nb}) = 0.07$  and 0.10 (Figs. 8f-j). If the  $x(\text{Nb}) = 0.02, 0.04, 0.07$  and 0.10 data are fit with an exponential,  $G_6(\vec{r}) = \exp(-\xi_6/r)$ , we obtain correlation lengths of  $\xi_6 \approx 200, 100, 11,$  and 5 lattice constants, respectively. A better fit to  $G_6(r)$  for  $x(\text{Nb}) = 0.02, 0.04$  is obtained, however, using an algebraic decay,  $G_6(\vec{r}) = r^{-\eta}$ , with  $\eta = 0.03$  and 0.12, respectively.

The simultaneous observation of long range orientational order and short range translational order in the  $x(\text{Nb}) = 0.02$  and 0.04 samples is strongly suggestive of the hexatic state that arises in 2D melting driven by topological defects.<sup>36</sup> 2D melting theory, which is based on equilibrium statistical mechanics, predicts that melting is a continuous phase transition between (1) a crystalline solid phase that has long range translational and orientational order:  $G_T(\vec{r}) \sim r^{-\xi}$ ,  $G_6(\vec{r}) \sim 1$ ; (2) a hexatic phase that has short range translational order but long range orientation order:  $G_T(\vec{r}) = e^{-r/\xi_T}$ ,  $G_6(\vec{r}) \sim r^{-\eta}$ ; and (3) a liquid phase that has short range translational and orientational order:  $G_T(\vec{r}) = e^{-r/\xi_T}$ ,  $G_6(\vec{r}) = e^{-r/\xi_6}$ . Our data show similar behavior and thus we suggest that the CDW lattice evolves from crystalline ( $x=0$ ) to hexatic ( $x=0.02-0.04$ ) to amorphous ( $x \geq 0.07$ ) states.

## Section-5

### Summary

Scanning tunneling microscopy (STM) and atomic force microscopy (AFM) have been used to characterize the atomic level structure of electronic properties, reactivity and wear of metal dichalcogenide materials that are or have potential as solid state lubricants. Single crystals of  $\text{MoS}_2$ ,  $\text{Ni}_x\text{Mo}_{1-x}\text{S}_2$ ,  $\text{MoS}_{2-x}\text{Se}_x$  and  $\text{MoS}_{2-x}\text{Te}_x$  have been prepared to determine how chemical modifications affect the local structure and electronic properties of this lubricant. STM images of Ni-doped  $\text{MoS}_2$  show localized electronic states due to the Ni atoms, while images of Se- and Te-doped materials indicate that anion substitution is electronically delocalized. AFM studies of Te-doped  $\text{MoS}_2$  show, however, that the tellurium dopants form atomic scale structural protrusions that may reduce sliding friction.

AFM has also been used to characterize nanometer scale wear and oxidation on  $\text{MoS}_2$  and  $\text{NbSe}_2$  surfaces. In atmosphere at room-temperature AFM studies showed that  $\text{NbSe}_2$  wears approximately three times faster than  $\text{MoS}_2$ . Furthermore, oxidation studies demonstrated that  $\text{NbSe}_2$  was significantly more reactive than  $\text{MoS}_2$  with molecular oxygen. These results indicate that the intrinsic stability of the  $\text{MoS}_2$  surface make it an effective lubricant. AFM was also used to elucidate the growth of  $\text{MoO}_3$  on the surface of  $\text{MoS}_2$  during oxidation, and to study wear properties of these  $\text{MoO}_3$  crystallites. The AFM tip was used to define lines with 10 nm resolution in  $\text{MoO}_3$  and to manipulate distinct  $\text{MoO}_3$  structures on the  $\text{MoS}_2$  surface.

In addition, metal-substitution in  $\text{TaS}_2$  has been studied systematically using STM and theoretical methods. Investigations of Nb-doped materials provide the first direct structural evidence for weak pinning of an electronic lattice, and furthermore, theoretical analyses have led to the discovery of a new phase, the hexatic, in these materials.

**Section-6**

**ACKNOWLEDGMENTS**

We gratefully acknowledge the support of this project under the direction of Col. Thomas Erstfeld. Major contributions to the research were made by Y. Kim, S. Kelty, H. Dai and J. Huang.

## References.

1. W.O. Winter, *Wear* **10**, 422 (1967).
2. W.E. Jamison, *ASLE Trans.* **15**, 296 (1972).
3. W.E. Jamison, *Proc. 3rd ASLE Int. Solid Lubrication Conf., Denver, CO*, in ASLE (American Society of Lubrication Engineers, New York) SP-14, p. 73 (1984).
4. P.D. Fleischauer, *Thin Solid Films* **154** 309 (1987).
5. T. Spalvins, *J. Vac. Sci. Technol. A* **5**, 212 (1987).
6. E. W. Roberts, *Proc. Inst. Mech. Eng., London* **1**, 503 (1987).
7. J.K.G. Panitz, L.E. Pope, J.E. Lyons and D.J. Staley, *J. Vac. Sci. Technol. A* **6**, 1166 (1988).
8. M.R. Hilton and P.D. Fleischauer, *J. Mater. Res.* **5**, 406 (1990).
9. X. L. Wu and C. M. Lieber, *J. Am. Chem. Soc.* **110**, 5200 (1988).
10. X. L. Wu, P. Zhou and C. M. Lieber, *Nature (London)* **335**, 55 (1988).
11. X. L. Wu, P. Zhou and C. M. Lieber, *Phys. Rev. Lett.* **61**, 2604 (1988).
12. X. L. Wu and C. M. Lieber, *Science (Washington)* **243**, 1703 (1989).
13. X. L. Wu and C. M. Lieber, *J. Am. Chem. Soc.* **111**, 2731 (1989).
14. X. L. Wu and C. M. Lieber, *Phys. Rev. B*, **41**, 1239 (1990).
15. X. L. Wu and C. M. Lieber, *Phys. Rev. Lett.*, **64**, 1150 (1990).
16. H. Chen, X. L. Wu, and C. M. Lieber, *J. Am. Chem. Soc.* **112**, 3326 (1990).
17. H. Chen, X. L. Wu, and C. M. Lieber, *Proceedings Air Force Tribology Technical Review*, in press.
18. X. L. Wu and C. M. Lieber, *Prog. Inorg. Chem.* **39**, 431 (1991).
19. X. L. Wu and C. M. Lieber, *J. Vac. Sci. & Technol. B* **9**, 1044 (1991).
20. H. Dai, H. Chen, and C. M. Lieber, *Phys. Rev. Lett.* **66**, 3183 (1991).
21. C. M. Lieber and X. L. Wu, *Acc. Chem. Res.* **24**, 170 (1991).
22. C. M. Lieber and Y. Kim, *Thin Solid Films* **206**, 355 (1991).
23. Y. Kim and C. M. Lieber, *Science*, **257**, 375 (1992).

24. H. Dai and C.M. Lieber, *Phys. Rev. Lett.* **69**, 1576 (1992).
25. J.-L. Huang, Y.-E. Sung and C.M. Lieber, *Appl. Phys. Lett.* **61**, 1528 (1992).
26. H. Dai and C.M. Lieber, *J. Phys. Chem.* **97**, 2362 (1993).
27. C.M. Lieber and Y. Kim, *Adv. Mat.* **5**, 392 (1993).
28. H. Dai and C.M. Lieber, *Ann. Rev. Phys. Chem.* **44**, 237 (1993).
29. Y. Kim, J.-L. Huang, and C.M. Lieber, *Appl. Phys. Lett.* **59**, 3404 (1991).
30. C.M. Lieber, in *The Technology of Proximal Probe Lithography*, to be published.
31. (a) G. Gruner, *Rev. Mod. Phys.* **60**, 1129 (1988). (b) G. Gruner and A. Zetl, *Phys. Rep.* **119**, 117 (1985).
32. (a) H. Fukuyama and P.A. Lee, *Phys. Rev. B* **17**, 535 (1978). (b) P.A. Lee and T.M. Rice, *Phys. Rev. B* **19**, 3970 (1979).
33. E. Sweetland, C.-Y. Tsai, B.A. Wintner, J.D. Brock, and R.E. Thorne, *Phys. Rev. Lett.* **65**, 3165 (1990).
34. (a) J.R. Tucker, *Phys. Rev. Lett.* **65**, 270 (1990). (b) J.C. Gill, *Phys. Rev. Lett.* **65**, 271 (1990).
35. R.E. Thorne and J. McCarten, *Phys. Rev. Lett.* **65**, 273 (1990).
36. (a) B.I. Halperin and D.R. Nelson, *Phys. Rev. Lett.* **4**, 121 (1978). (b) D.R. Nelson and B.I. Halperin, *Phys. Rev. B* **19**, 2457 (1979).
37. S.-K. Ma, *Modern Theory of Critical Phenomena* (Benjamin/Cummings, Reading, 1976).
38. F.R.N. Nabarro, *Theory of Dislocations* (Clarendon, Oxford, 1967).
39. G. F. Voronoi, *J. Reine Angew. Math.* **134**, 198 (1908).
40. Y. Imry, and S.-K. Ma, *Phys. Rev. Lett.* **35**, 1399 (1975).